Journal of Biomechanics 94 (2019) 49–58

Contents lists available at ScienceDirect

Journal of Biomechanics

journal homepage: www.elsevier.com/locate/jbiomech
www.JBiomech.com

Estimation of valvular resistance of segmented aortic valves using computational fluid dynamics

M.J.M.M. Hoeijmakers [a,b,*], D.A. Silva Soto [c], I. Waechter-Stehle [d], M. Kasztelnik [e], J. Weese [d], D.R. Hose [c], F.N. van de Vosse [a]

[a] Department of Biomedical Engineering, Eindhoven University of Technology, PO Box 513, 5600 MB Eindhoven, the Netherlands
[b] ANSYS France, 69100 Villeurbanne, France
[c] Department of Infection, Immunity and Cardiovascular Disease, University of Sheffield, Medical School, Beech Hill Road, S10 2RX Sheffield, United Kingdom
[d] Philips Research Laboratories, Röntgenstrasse 24-26, D-22335 Hamburg, Germany
[e] Academic Computer Centre Cyfronet, AGH, University of Science and Technology, Kraków, Poland

ARTICLE INFO

Article history:
Accepted 9 July 2019

Keywords:
Aortic valve stenosis
Heart valve disease
Hemodynamics
Computational fluid dynamics
Patient-specific

ABSTRACT

Aortic valve stenosis is associated with an elevated left ventricular pressure and transaortic pressure drop. Clinicians routinely use Doppler ultrasound to quantify aortic valve stenosis severity by estimating this pressure drop from blood velocity. However, this method approximates the peak pressure drop, and is unable to quantify the partial pressure recovery distal to the valve. As pressure drops are flow dependent, it remains difficult to assess the true significance of a stenosis for low-flow low-gradient patients. Recent advances in segmentation techniques enable patient-specific Computational Fluid Dynamics (CFD) simulations of flow through the aortic valve. In this work a simulation framework is presented and used to analyze data of 18 patients. The ventricle and valve are reconstructed from 4D Computed Tomography imaging data. Ventricular motion is extracted from the medical images and used to model ventricular contraction and corresponding blood flow through the valve. Simplifications of the framework are assessed by introducing two simplified CFD models: a truncated time-dependent and a steady-state model. Model simplifications are justified for cases where the simulated pressure drop is above 10 mmHg. Furthermore, we propose a valve resistance index to quantify stenosis severity from simulation results. This index is compared to established metrics for clinical decision making, i.e. blood velocity and valve area. It is found that velocity measurements alone do not adequately reflect stenosis severity. This work demonstrates that combining 4D imaging data and CFD has the potential to provide a physiologically relevant diagnostic metric to quantify aortic valve stenosis severity.

© 2019 Elsevier Ltd. All rights reserved.

1. Introduction

Aortic valve stenosis (AS) is the narrowing of the aortic valve and disturbs blood flow into the systemic circulation. Once developed, AS consistently increases with age, and it is estimated that 2.8–3.9% of the population older than 70 years of age suffer from some form of AS (Eveborn et al., 2012; Nkomo et al., 2006). AS is often caused by calcification of the Aortic Valve (AV) leaflets, resulting in a stiffer valve that impedes the opening and closing function of the valve. Hence, in systole, the valve may not open completely, and a large pressure difference is required to maintain flow. If left untreated, AS may eventually lead to heart failure.

AS disturbs flow from the ventricle into the aorta, and a large effective pressure difference is required to maintain cardiac output. The drop in pressure is an indicator for the severity of AS. However, non-invasive diagnostic quantitative evaluation of the pressure drop is challenging. Hence, in current clinical practice other indirect metrics are used. At present, the main criteria to judge AS severity are: the mean transaortic pressure drop; maximum velocity of the jet (v_{max}), and the Aortic Valve Area (AVA) by continuity equation (Chambers, 2016; Nishimura et al., 2014; Baumgartner et al., 2016). All these metrics are routinely obtained by echocardiography. However, v_{max} and the mean pressure drop are both flow-dependent, and may conflict with AVA measurements for approximately 20–30% of patients with severe AS (Eleid et al., 2013). For this patient group it remains difficult to assess whether AS is significantly present (Vogelgesang et al., 2017).

* Corresponding author at: Eindhoven University of Technology, De Rondom 70, Eindhoven, the Netherlands.
E-mail address: m.j.m.m.hoeijmakers@tue.nl (M.J.M.M. Hoeijmakers).

https://doi.org/10.1016/j.jbiomech.2019.07.010
0021-9290/© 2019 Elsevier Ltd. All rights reserved.

Echocardiography is inexpensive, readily available and easy to perform, and an established method to derive metrics indicative of stenosis severity. When echocardiography results are inconclusive, Computed Tomography (CT) or cardiac Magnetic Resonance Imaging (MRI) can be used to derive additional indicators, e.g the aortic diameter or amount of calcification (Chun et al., 2008). Furthermore, CT and cardiac MRI enable detailed three-dimensional reconstructions of the full-heart anatomy. Moreover, segmentation methods from cardiac CT and MRI images have improved considerably over the past years (Ecabert et al., 2008, 2011; Grbic et al., 2012; Ionasec et al., 2010). Furthermore, recent developments see high-quality valve models incorporated into existing segmentation frameworks (Weese et al., 2017). These detailed 3D models of the AV can be used in combination with 3D Computational Fluid Dynamics (CFD) to evaluate the hemodynamic performance of the patient-specific valve (Weese et al., 2017). However, in order to quantify the load on the ventricle, extending the CFD model to include the (contracting) Left Ventricle (LV) may yield information on the true significance of the stenotic valve.

In systole, a healthy valve opens completely, and imposes little to no resistance to blood flow. However, flow through the diseased valve is similar to flow through an orifice. Blood is accelerated into the orifice, and pressure is converted to kinetic energy. When blood enters the Ascending Aorta (AA), it is decelerated, and pressure is partly recovered (Fig. 1). Pressure is not completely recovered due to viscous losses, including those from turbulence. This results in an effective pressure drop between the LV and AA. To quantify the relative contribution of the valve to the effective pressure drop, a valve resistance index is proposed:

$$I_{VR} = \frac{\Delta P_V}{\Delta P_E} \tag{1}$$

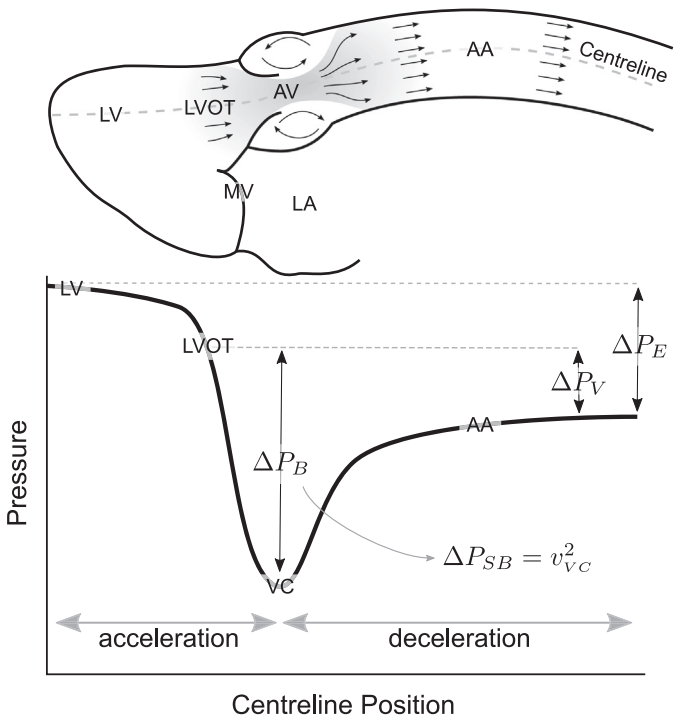

Fig. 1. Top: schematic of the Left Ventricle (LV), Left Ventricular Outflow Tract (LVOT), Aortic Valve (AV), Vena Contracta (VC) and Ascending Aorta (AA). Bottom: typical pressure along the centreline. ΔP_V: net pressure drop across the AV. ΔP_E: effective pressure drop between the LV and AA. ΔP_B: Bernoulli estimate, i.e. the maximum pressure drop across the valve, ΔP_{SB}: simplified Bernoulli estimate from VC velocity. Mitral Valve (MV) and Left Atrium (LA) are added for anatomical reference.

This index quantifies the pressure loss due to the presence of the valve (ΔP_V) with respect to the total effective pressure loss between the LV and AA (ΔP_E). For healthy valves, pressure is expected to recover approximately to the same pressure level as in the Left Ventricular Outflow Tract (LVOT). When the cross-sectional area of the AA exceeds that of the LVOT, blood velocity (and kinetic energy) in the AA decrease. Consequently, (static) pressure may recover beyond LVOT pressure. However, for diseased valves, it is expected that only a (small) part of pressure is recovered, and excessive viscous and turbulent losses dominate.

The main aim of this work is to evaluate the valve resistance index proposed in Eq. 1 with clinically accepted measures, such as, v_{max} and the AVA. Additionally, the CFD model with the contracting left ventricle is used to evaluate the accuracy of simplified valve-only CFD models and Bernoulli approximations. For this purpose, the workflow described by Weese et al. (2017) is extended to include both the AV and contracting ventricle.

2. Materials and methods

2.1. Aortic valve anatomies

Cardiac CT segmentation data was obtained from an anonymized dataset used in a previous study (Weese et al., 2017). Original images were acquired using electrocardiogram-gated CT angiography with 10% intervals of the electrocardiographic R-R interval. CT images had an in-plane resolution of 0.31–0.68 mm and slice thickness of 0.34–0.70 mm. Segmented anatomical structures include the LV, LVOT and AV. Fig. 2B shows a typical segmented anatomy at different phases of the cardiac cycle.

Surface models of the LV and AV throughout systole were generated for each patient with a Shape Constrained Deformable Model (SCDM). The authors refer to Ecabert et al. or Weese et al. for a detailed description of the SCDM (Ecabert et al., 2008; Ecabert et al., 2011; Weese et al., 2017). The surface model at mid-systole was selected, and developed into the CFD model. This model had the valve in the most open position, typically at 20% or 30% of the electrocardiographic R-R interval. The surface model consisted of 3094 vertices and 6169 triangles with an average edge length of 2.6 mm (Fig. 2B). The geometric AVA was estimated from the structured surface model by a projection method (Weese et al., 2017). All segmentation surface models throughout the cardiac cycle were then converted into binary masks, covering the LV and LVOT, to facilitate registration.

2.2. Image registration

Each consecutive binarized image pair was registered using The Sheffield Image Registration Toolkit (Barber and Hose, 2005). The resulting 3D discrete mapping fields morphed one image onto the next. The Sheffield Image Registration Toolkit produced smooth, non-linear registration maps with sub-pixel accuracy. To compute the 3D mappings between the images, the Sheffield Image Registration Toolkit uses an intensity-based linear least-squares algorithm, iteratively applied to handle large displacements. The 3D registration map was spatially interpolated to the vertices of the surface model at mid-systole. This yielded a set of surface models in the R-R interval with the same topology as the surface model at mid-systole. Registration was done on the binarized images, hence no information on the motion of the AV and AA was available. For this reason, and for CFD stability the mean rigid motion of the model was removed from the overall model motion. Velocity vectors $\vec{v}$ for each vertex n of the surface model were a function of time and computed from the consecutive iso-topological surface models by:

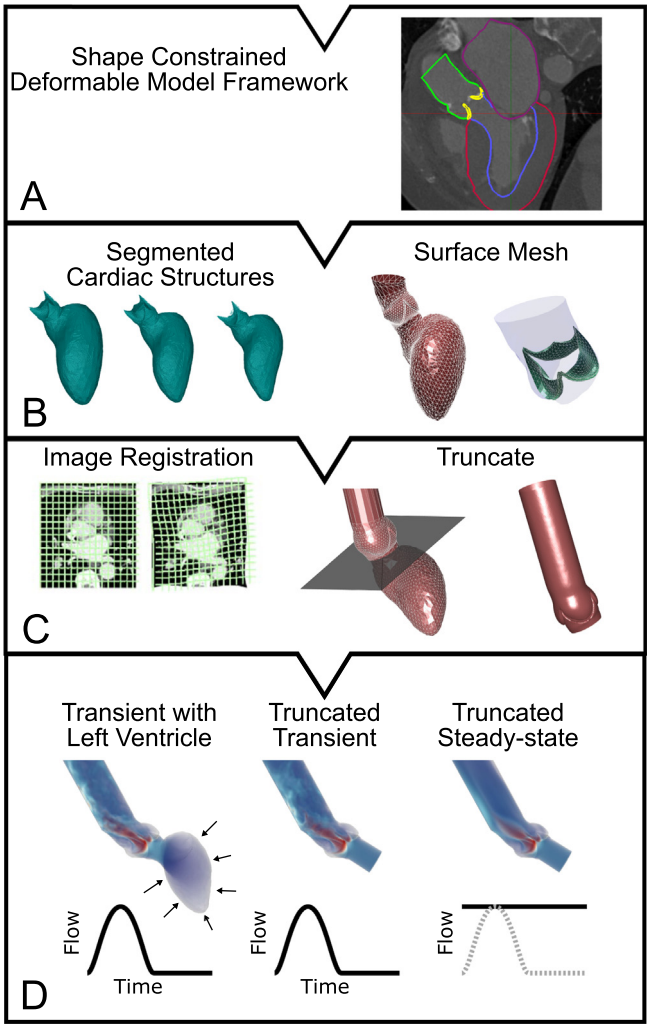

Fig. 2. Illustration of the workflow from (A) the Shape Constrained Deformable Model framework (Ecabert et al., 2011; Weese et al., 2017); (B) segmented aortic valve and left ventricle and corresponding surface model; (C) image registration and mesh truncation; (D) 4D CFD Model of the AV and contracting ventricle, 3D truncated transient model, and 3D truncated steady-state model.

$$\vec{v}_n(t) = \frac{\vec{x}_n(t+\Delta t) - \vec{x}_n(t)}{\Delta t} \tag{2}$$

With $\vec{x}$ the position of vertex n at time t in the cardiac cycle. Vertex positions were sparse in time, and were interpolated using cubic splines.

2.3. Mesh generation

Volumetric meshing was performed with ANSYS Fluent Meshing R17.2 (ANSYS Inc, Canonsburg, Pennsylvania, United States). Structured surface models were truncated at the LVOT by a manually defined plane two to five mm proximal to the valve annulus and orthogonal to the valve axis (Fig. 2C). The outflow boundary was extended by 3.5 times the diameter of the AA. The inflow boundaries of the truncated models were extended by 1.5 times the LVOT diameter. The volume was filled with tetrahedra in the core, and ten layers of pentahedra elements inflated from the wall. Element sizes were chosen based on a mesh sensitivity study, and ranged between 0.5 and 2.5 mm. Maximum element edge length in the LV was constrained to 2.5 mm. Edge lengths in the proximity of the AV were constrained to 0.5 mm to capture valve features.

2.4. Computational methods

Fluid flow is governed by the Navier-Stokes equations. For moving grids, the integral form of the continuity equation for a control volume Ω with surface Γ can be written as.

$$\frac{\partial}{\partial t}\int_\Omega \rho dV + \int_\Gamma \rho(\vec{v} - \vec{v}_g)\cdot\vec{n}dA = 0 \tag{3}$$

With ρ the density of blood, $\vec{v}$ the velocity vector, $\vec{v}_g$ the velocity of the (boundary) grid, and $\vec{n}$ the normal vector to the surface Γ. Similarly, the momentum equation can be written as:

$$\frac{\partial}{\partial t}\int_\Omega (\rho\vec{v})dV + \int_\Gamma \rho\vec{v}(\vec{v} - \vec{v}_g)\cdot\vec{n}dA = -\int_\Gamma p\mathbf{I}\cdot\vec{n}dA + \int_\Gamma \boldsymbol{\tau}\cdot\vec{n}dA \tag{4}$$

where p is the pressure, $\mathbf{I}$ the identity tensor, and $\boldsymbol{\tau}$ the viscous stress tensor. A diffusion based smoothing method was applied for grid motion.

$$\nabla\cdot(\gamma\nabla\vec{v}_g) = 0 \tag{5}$$

$$\gamma = \frac{1}{d^\alpha} \tag{6}$$

With $\vec{v}_g$ the grid velocity, γ the diffusion coefficient and d the normalized distance to the boundary. For all simulations $\alpha = 1$ and resulted in skewed grid motion towards the interior, i.e. elements in the interior deformed more. The boundary conditions (Fig. 3) for the diffusion equation were:

$$\begin{aligned} &\Gamma_{AA}, \Gamma_{Sinus}, \Gamma_{AV} &&: \vec{v}_g = 0 \\ &\Gamma_{LVOT} &&: \vec{v}_g = f(s)\vec{v}_n(t) \\ &\Gamma_{LV} &&: \vec{v}_g = \vec{v}_n(t) \end{aligned}$$

Here $f(s)$ is a ramp function that linearly scaled boundary velocity to zero in the LVOT as a function of the position s in the LVOT, i.e. $f(s) = 1$ at the side of the LV, and $f(s) = 0$ towards the valve.

Blood was modeled as an in-compressible fluid with a density of 1050 kg·m^{-3} and dynamic viscosity of 0.004 Pa·s. No-slip boundary conditions were assumed at the walls, and at boundary Γ_{out} pressure is set to zero. The governing equations were solved with ANSYS Fluent R17.2 (ANSYS Inc, Canonsburg, Pennsylvania, United

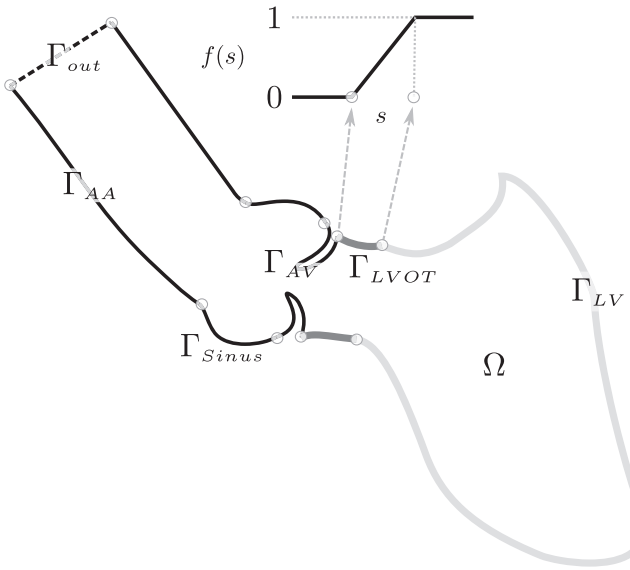

Fig. 3. Boundary and domain definitions. Boundaries Γ_{LV} (light gray line) and Γ_{LVOT} (dark gray line) are deforming. Γ_{AV}, Γ_{Sinus}, Γ_{AA} (black lines) and Γ_{out} (dashed line) are static boundaries, i.e. $\vec{v}_g$ is zero. Boundary motion is scaled to zero in the LVOT by a ramp function $f(s)$, with s the position in the LVOT.

States). Simulations were executed on the ACC Cyfronet AGH Prometheus Supercomputer (Academic Computer Centre Cyfronet, AGH University of Science and Technology, Kraków, Poland). Each simulation was assigned one compute node with 24 CPU's.

2.4.1. Transient models

For the transient models a (bounded) central difference scheme was used for the advection and diffusion terms. The transient term was integrated with a second order backward difference approximation. Convergence criteria at each time-step were set at 0.05 for locally scaled residuals of x-, y-, z-velocity, and continuity. Sub-grid turbulent dissipation was modeled with Large Eddy Simulation and the Wall Adapting Local Eddy-Viscosity model (Nicoud and Ducros, 1999). Time steps were defined as 1/10,000th of the cardiac cycle. Vertex velocities were spatially interpolated from the structured surface model onto the re-meshed surface of the computational domain by an inverse distance-weighted interpolation using eight nearest neighbors of the structured model. Stroke volume was pre-computed with a discrete form of Gauss's theorem (Hughes et al., 1996) for the structured and re-meshed surfaces. Vertex velocities of the refined computational mesh were scaled to match the stroke volume of the structured surface model. The time-dependent grid velocity was applied to the boundary of the LV and LVOT. For the truncated model, the pre-computed flow waveform was used as a time-dependent plug-flow boundary condition. To test whether diastolic filling of the ventricle had to be simulated, five cardiac cycles were simulated for case 11. Results in Table 1 demonstrate that diastolic filling had a negligible ($< 1\%$) effect on the observed peak-systolic pressure drop and valve resistance index. Hence, diastolic filling was neglected, and only a single systolic cycle was simulated to restrict the computational burden.

2.4.2. Steady-state model

Peak flow-rate was obtained from the pre-computed flow waveform, and prescribed as a boundary condition for the truncated steady-state model. Turbulence is modeled with the Shear Stress Transport $k-\omega$ model (Menter, 1994).

2.5. Post-processing

A centreline with equally spaced points (0.1 mm intervals) was defined for each surface model with the Vascular Modelling Toolkit (Antiga et al., 2008). Pressure was evaluated on the centreline, and the effective (ΔP_E) and valve (ΔP_V) pressure-drops were computed. These pressure drops were used to compute the valve resistance index I_{VR} (Eq. 1). Furthermore, Bernoulli estimates ($\Delta P_B = P_{LVOT} - P_{VC}$) and simplified Bernoulli estimates ($\Delta P_{SB} = 4v_{VC}^2$) were computed from the simulation results. Note that v_{VC} is the velocity at the vena contracta, and corresponds to v_{max}. The point on the centreline closest to the truncation plane was used to evaluate P_{LVOT}. The vena contracta was identified by inspecting the centreline, i.e. where pressure was lowest.

3. Results

The workflow described in Fig. 2 was used on retrospective CT datasets of 18 patients with non-calcified and (partially) severely calcified tricuspid AV's (Fig. 4). Projected AVA ranged between 0.9 and 4.3 cm^2 (Table 2). Image derived maximum flow rate at

Table 1
Pressure drop results over multiple cardiac cycles for case 11.

	Cycle 1	Cycle 2	Cycle 3	Cycle 4	Cycle 5
P_{LV} [mmHg]	6.86	6.90	6.89	6.88	6.94
P_{LVOT} [mmHg]	3.42	3.44	3.43	3.43	3.49
I_{VR} [–]	0.499	0.499	0.498	0.498	0.503

Note: simulations performed with a time-step of $1 \cdot 10^{-3}$ s to limit simulation times.

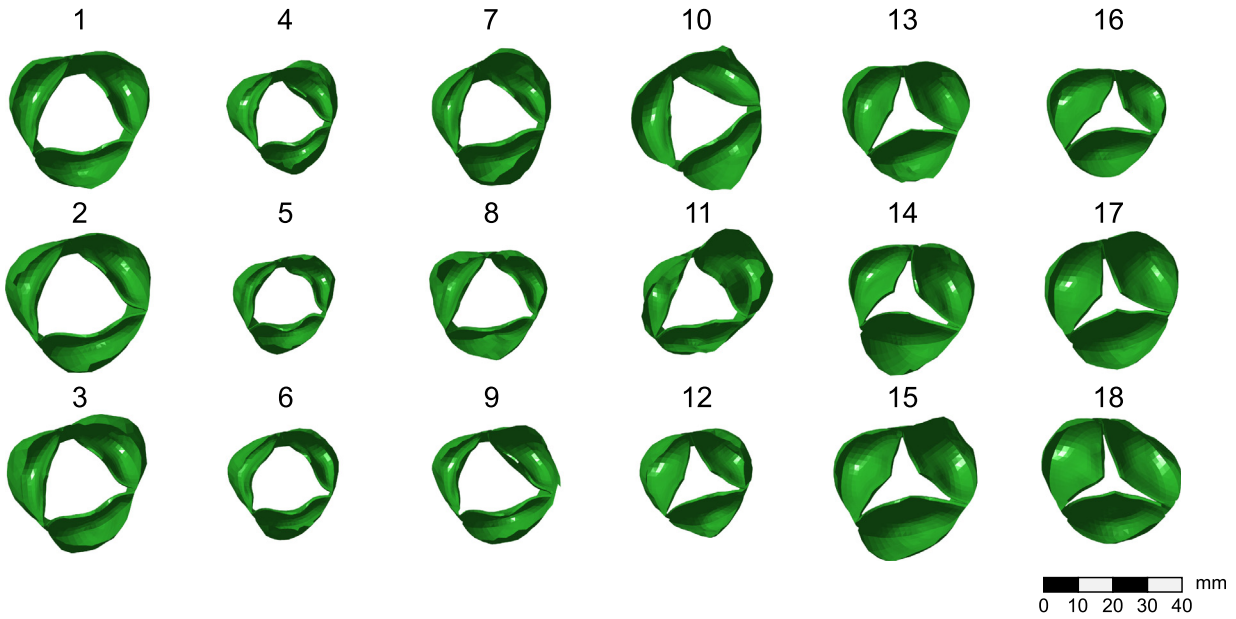

Fig. 4. Axial view of the segmented AV for all cases. Cases 1–9 have a $I_{VR} < 0.25$, cases 10 and 11 $0.25 < I_{VR} < 0.75$, and cases 12–18 a $I_{VR} > 0.75$. Case numbering corresponds to Table 2.

Table 2
Pressure drop estimates for each case and all models, ordered by valve resistance index.

Case	HR bpm	A_{LVOT} cm^2	A_{AV} cm^2	A_{AA} cm^2	Q_{max} ml/s	v_{max} m/s	ΔP_E^{CLV} mmHg	ΔP_V^{CLV} mmHg	ΔP_V^{TT} mmHg	ΔP_V^{TS} mmHg	ΔP_B^{CLV} mmHg	ΔP_{SB}^{CLV} mmHg	∇P_{LVOT}^{CLV} mmHg/mm	I_{VR}[a] −2 mm	I_{VR}	I_{VR}[b] +2mm
1	73	4.8	3.9	10.1	489	1.47	5.7	−2.3	−1.4	0.4	1.7	8.6	−0.20	−0.33	−0.40	−0.47
2	56	5.5	4.3	14.7	433	1.14	3.4	−1.1	−0.6	0.4	1.2	5.2	−0.11	−0.25	−0.32	−0.39
3	66	4.6	3.3	9.5	397	1.33	4.6	−0.7	0.1	1.4	2.5	7.1	−0.15	−0.09	−0.15	−0.22
4	58	3.4	2.4	7.2	330	1.64	8.4	−0.2	0.4	1.2	3.3	10.8	−0.28	0.04	−0.02	−0.09
5	87	3.1	2.3	7.4	178	0.88	2.5	−0.1	0.1	0.4	1.0	3.1	−0.07	0.03	−0.02	−0.08
6	63	4.3	2.7	6.7	321	1.33	5.4	0.2	0.9	1.3	2.3	7.1	−0.18	0.09	0.03	−0.04
7	66	4.1	2.8	7.8	451	1.81	8.8	0.3	1.5	2.8	4.9	13.1	−0.25	0.09	0.03	−0.03
8	61	4.3	2.7	9.5	415	1.75	9.1	1.3	1.5	2.4	4.8	12.2	−0.32	0.21	0.14	0.07
9	66	4.5	3.2	10.2	488	1.76	9.0	1.6	1.4	2.9	5.4	12.4	−0.29	0.24	0.18	0.11
10	63	5.1	3.0	11.1	635	2.39	18.0	6.8	6.0	7.5	12.5	22.8	−0.70	0.45	0.37	0.30
11	67	4.5	2.3	12.1	296	1.42	6.8	3.3	3.5	3.6	5.0	8.1	−0.19	0.53	0.48	0.42
12	66	3.9	1.3	8.5	416	3.47	41.7	31.8	32.6	32.9	38.4	48.1	−0.63	0.79	0.76	0.73
13	74	3.8	1.2	9.3	510	4.40	65.2	50.0	53.7	52.3	63.0	77.5	−0.46	0.78	0.77	0.75
14	80	3.6	1.3	9.5	417	3.47	40.2	31.6	30.6	31.1	39.8	48.2	−0.40	0.81	0.79	0.77
15	82	5.8	1.6	11.9	302	1.97	12.6	10.6	10.7	11.5	13.2	15.5	−0.26	0.88	0.84	0.79
16	98	4.0	1.1	8.3	286	2.75	26.6	22.8	22.4	22.7	26.3	30.3	−0.26	0.88	0.86	0.84
17	57	4.7	1.0	10.9	511	5.36	102.5	91.5	89.5	89.8	103.2	115.1	−0.77	0.91	0.89	0.88
18	74	5.6	0.9	8.1	251	3.16	36.4	34.9	33.9	34.3	38.0	39.9	−0.19	0.97	0.96	0.95

[a] Valve resistance index when P_{LVOT} is taken 2 mm upstream of truncation plane.
[b] Valve resistance index when P_{LVOT} is taken 2 mm downstream of truncation plane.

peak systole range between 178 and 635 ml/s, and simulated velocities in the vena contracta range between 0.88 and 5.36 m/s. The effective pressure drop ΔP_E^{CLV} ranges between 2.5 and 102.5 mmHg. Net pressure drops across the aortic valve range between: −2.3 mmHg and 91.5 mmHg for the full model; −1.4 mmHg and 89.5 mmHg for the truncated transient model; 0.4 mmHg and 89.8 mmHg for the steady-state model. ΔP_B^{CLV} and ΔP_{SB}^{CLV} range between 1.0–103.2 mmHg and 3.1–115.1 mmHg. The valve resistance index lies between −0.40 and 0.96. The local pressure gradient in the LVOT was between −0.77 and −0.07 mmHg/mm.

Fig. 5 illustrates the CFD results of a healthy (case 8) and a stenotic valve (case 17). The healthy case exhibits a lower jet velocity through the AV than the stenotic case. For the stenotic valve a distinct jet is formed, and turbulent structures develop. The jet is wider and not as pronounced for the healthy valve. Pressure contours demonstrate that the the effective pressure drop between the LV and AA is about 9 mmHg for the healthy case and approximately 110 mmHg for the stenotic case.

Fig. 6 visualizes the relationship between v_{max} and the proposed valve resistance index. When assessing AS severity by v_{max}, 12 cases would be considered healthy, one case as having a mild stenosis, and three as having a moderate stenosis. Two cases would be classified as having a severe stenosis. Cases 15 and 16 would be classified as having no or a mild stenosis. However, both exhibit large valve resistance indices of 0.84 and 0.86 respectively, of similar magnitude as the clearly stenotic cases 13 and 17. Furthermore, it is observed that case 18, actually has the largest valve resistance index, but would have been classified as moderate with v_{max} as criteria. Healthy valves exhibit valve resistance indices close to or below zero. Furthermore, an inverse linear relationship between the geometric AVA and valve resistance index may be observed; when AVA decreases, the valve resistance index increases (Fig. 6).

Fig. 7A and B qualitatively demonstrate the differences between each of the CFD models. Unsteady flow phenomena distal to the AV are observed. Flow patterns for the transient models are similar, but local discrepancies in the velocity field can be noticed. Unsteady flow patterns propagate far into the AA for this particular stenotic case.

Qualitatively the shape of the jet and the pressure contours are similar proximal to and in the immediate vicinity of the valve for the steady-state and transient models (Fig. 7). However, flow structures distal to the valve are less well-matched. This is expected because the jet has had no time to develop fully in space for the transient models. Despite the loss of fidelity in the flow field, the steady-state model captures the overall pressure drop adequately. Pressures proximal to the AV, in the vena contracta and distal to the AV are approximately the same for all models.

Differences in ΔP_V of 0.3 ± 1.33 and 0.9 ± 1.63 are found between the transients models, and truncated steady and full model respectively (Fig. 8A and B). A bias of 0.7 ± 1.07 mmHg is observed between both truncated models (Fig. 8C). The simplified Bernoulli and full 4D CFD model are in poor agreement: a bias of 11.3 ± 6.6 mmHg (Fig. 9B). At low-flow the simplified Bernoulli equation provides a poor estimate of the peak-systolic effective pressure-drop. Bernoulli estimates demonstrate a bias of 6.6 ± 3.27 mmHg compared to the full model. In general, discrepancies from the full model predominantly occur at low pressure drops (Figs. 8 and 9). E.g., the relative difference between ΔP_V^{CLV} and ΔP_V^{TT} for case 6 is 140%. In contrast, a relative difference of only 2% is found for case 17.

4. Discussion

This paper presents a medical image-based CFD framework to simulate flow across a patient-specific AV. A valve resistance index is defined, and compared to measures typically used in the clinic to demonstrate the frameworks potential value. Additionally, the effect of model simplifications on pressure-drop computations are presented.

4.1. Sample characteristics

Computed geometric AVA's (Table 2) suggest that the current sample contains 11 healthy or mildly stenosed cases, six moderate cases, and one severe case (Nishimura et al., 2014). When considering v_{max} as severity index, it is found that 12 cases can be classified as healthy, one as mild, three as moderate, and two as having a severely stenotic valve. Unfortunately, no echocardiography or cardiac catheterization data was available to clinically classify the patients. Nevertheless, computed velocities, pressure-drops and AVA correspond well to values reported in literature (Chambers, 2016; Baumgartner et al., 1999). For example, cardiac catheterization and echocardiography measurements in AS patients by Yang

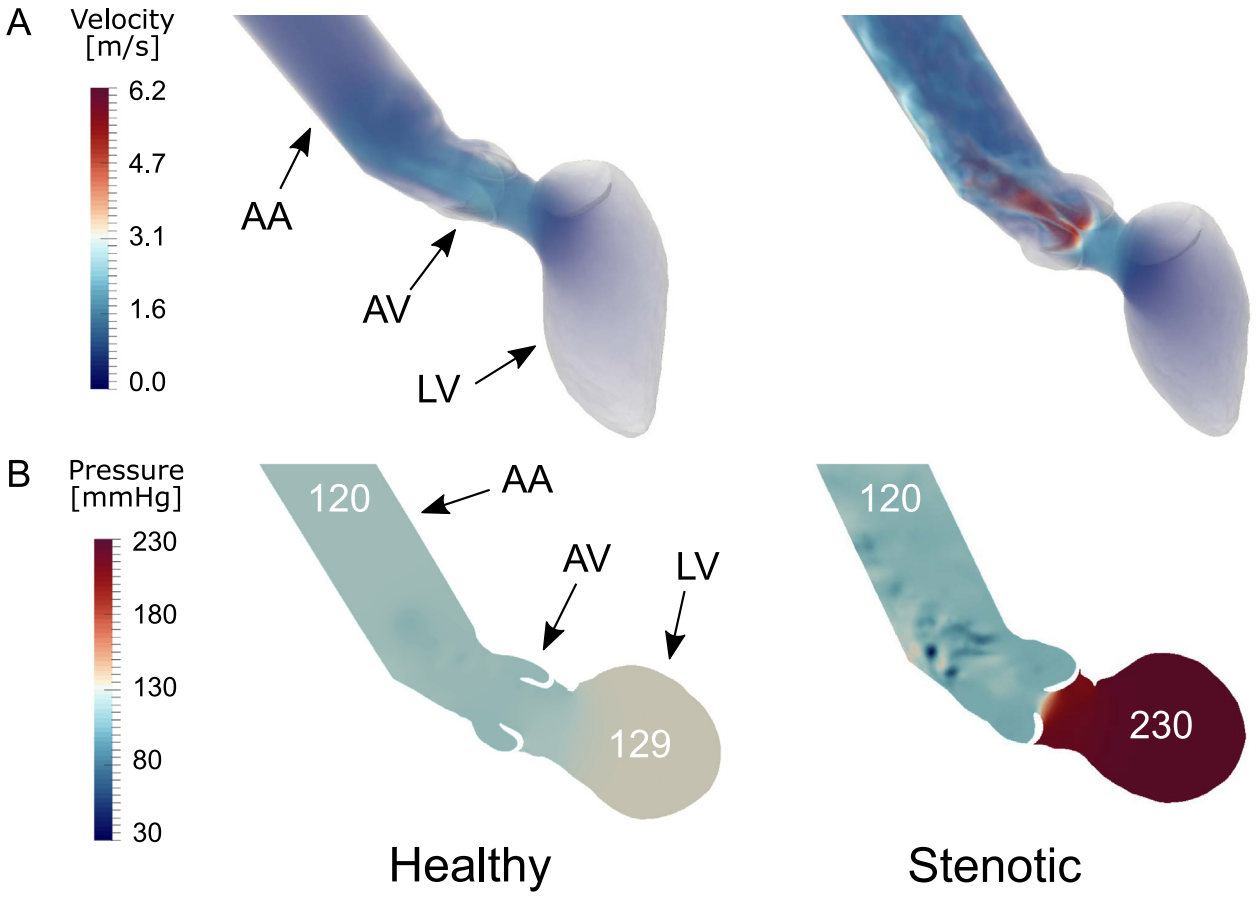

Fig. 5. Volume renders of velocity (A) and contour plots of pressure (B) at peak systole for a healthy valve (left – case 8) and a stenotic valve (right – case 17).

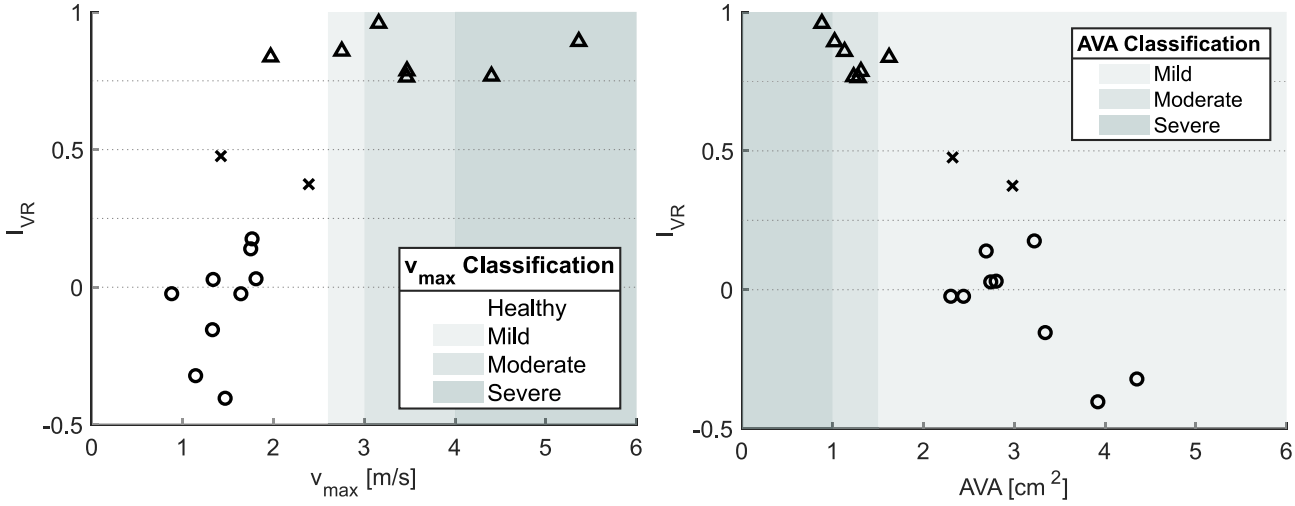

Fig. 6. Left: CFD derived v_{max} vs. valve resistance index. Severity classifications are based on guidelines (Nishimura et al., 2014). Healthy: $v_{max} < 2.6$ m/s. Mild: 2.6 m/s < v_{max} < 2.9 m/s, moderate: 3.0 m/s < v_{max} < 4.0 m/s, severe: $v_{max} > 4.0$ m/s. Right: geometric AVA vs. valve resistance index. Healthy/Mild: AVA > 1.5 cm^2, moderate: 1.0 cm^2 < AVA < 1.5 cm^2, severe AVA < 1.0 cm^2. Furthermore, cases are separated in groups, $I_{VR} < 0.25$ (○), $0.25 < I_{VR} < 0.75$ (×) and $I_{VR} > 0.75$ (△). Note that the reported AVA is the geometric projected AVA, and not the effective orifice area (by echocardiography) as reported in the guidelines (Nishimura et al., 2014).

et al. show systolic pressure drops between the LV and AA up to 129 mmHg for patients with (echocardiography derived) AVA's of 0.4 cm^2 (Yang et al., 2015). Furthermore, the same study reports echocardiography based peak-systolic v_{max} measurements of 2.3–5.2 m/s. The reported upper limits for ΔP_E and v_{max} in this study are 103 mmHg and 5.4 m/s, and thus respect the limits typically reported in literature.

4.2. Valve resistance index

The valve resistance index is a measure of how much pressure is lost due to the presence of the AV. This index can be interpreted as a percentage, e.g. an index of 0.60 means that 60% of pressure loss can be attributed to the AV. Fig. 6 demonstrates that healthy valves (cases 1–9) have valve resistance indices of around zero, i.e. any

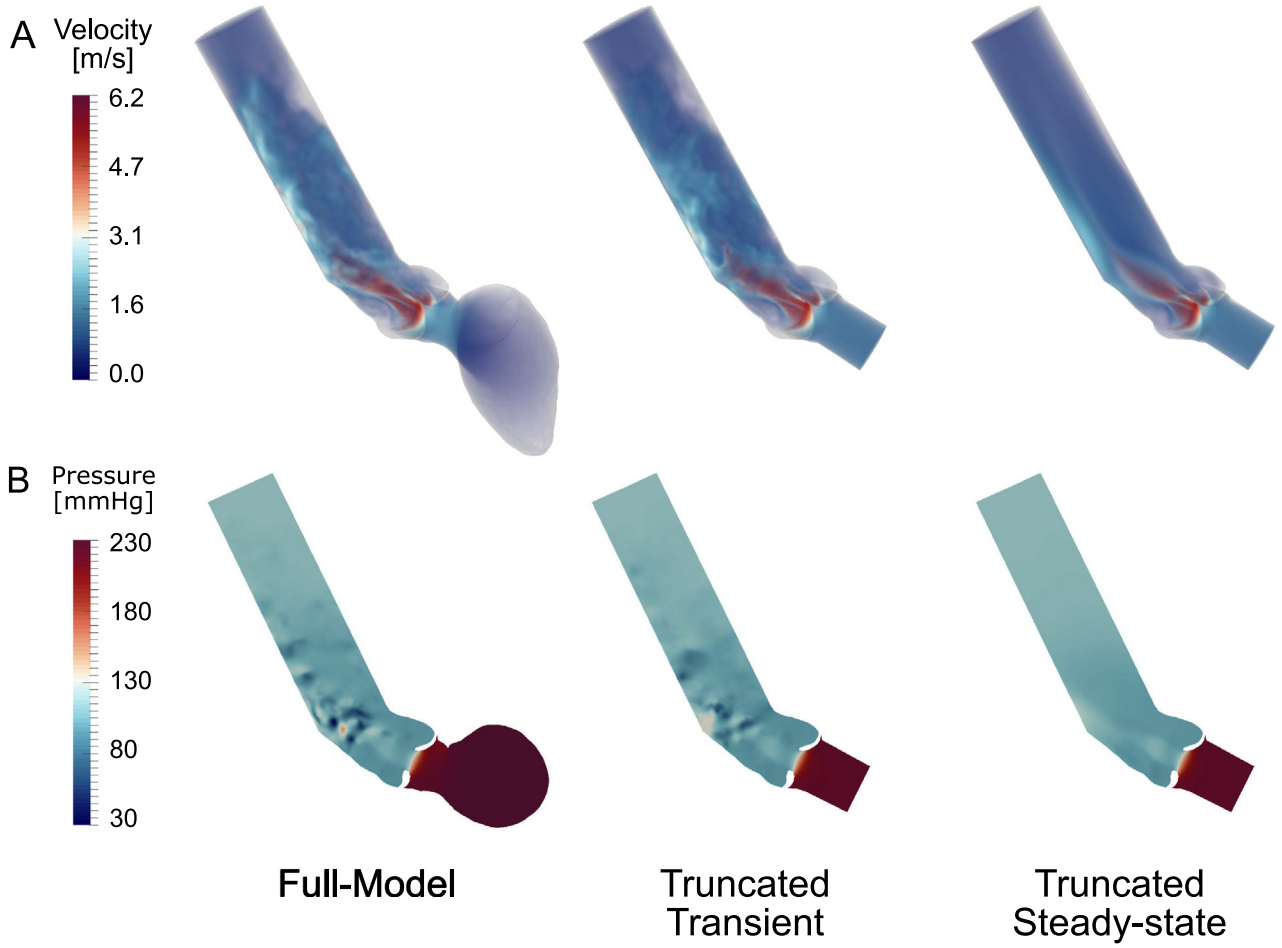

Fig. 7. Volume render of velocity magnitude (A) and pressure contours (B) for each of the CFD models.

pressure lost around the AV is fully recovered in the AA. For some cases, recovered pressure even exceeds pressure in the LVOT (cases 1–3). This can be explained by the fact that the cross-sectional area of the AA is typically two to three times larger than the cross-sectional area of the LVOT (see Table 2). Due to the larger cross-sectional area, velocity in the AA will be lower, and more kinetic energy is converted back into static pressure. Hence, pressure may recover beyond that of the LVOT, leading to a negative valve resistance index. Therefore, a healthy valve, in its open position, exerts no additional load on the left ventricle at peak systole. For severely stenotic valves, the valve dominates the effective pressure drop (cases 17 and 18), i.e. approximately 90% of the effective pressure drop is attributed to the AV. This is in line with numerical results presented by Traeger et al. (Traeger et al., 2015). Although not the main aim of their work, their illustrations suggest that a valve with an area of 0.9 cm^2 (Gorlin derived) may exhibit a valve resistance index of approximately 0.9 at flow rates of 200 and 400 ml/s.

Fig. 6 clearly demonstrates the inability of v_{max} to identify a stenosis consistently. Due to low-flow, cases 15 and 16 demonstrate a v_{max} that would be considered normal, or mildly stenotic in clinical practice. However, the valve resistance index for these cases reveals that – similar to other stenotic valves – the effective pressure drop is dominated by the AV. A disproportional amount of the pressure loss is due to the presence of the valve. Such a conclusion can not be drawn from v_{max} (Fig. 6) and ΔP_E measurements alone. Hence, for cases where AVA and v_{max} conflict, the valve resistance index may provide relevant information on stenosis severity.

4.3. Comparison CFD models

Qualitatively, no major differences are observed between the transient models (Fig. 7). Similar (turbulent) structures are formed distal to the AV where the jet breaks down, and pressure is recovered. Steady-state simulations demonstrate averaged velocity and pressure distributions, and do not capture local flow disturbances in detail. Nevertheless, steady-state simulations capture the global pressure drop across the AV within reasonable limits. Both truncated models provide acceptable estimates for the pressure drop across the AV. At low pressure drops (<10 mmHg) the truncated models overestimate the pressure drop considerably in the relative sense. An artificial plug-flow assumption at the inflow boundary may not be appropriate for cases that exhibit low pressure-drops. Indeed, velocity profiles in the LVOT are not plug-like (Garcia et al., 2011). Work by Bruening and colleagues shows that significant overestimation of the pressure drop can occur when assuming a plug-flow velocity profile opposed to a patient-specific flow profile from 4D velocity-encoded MRI (Bruening et al., 2018). However, differences between the full and truncated transient model are small in this study, and the added accuracy of the full model may therefore not outweigh the additional computational cost.

The simplified Bernoulli equation – normally derived from echocardiography measurements – overestimates the pressure drop substantially. Overestimation of the pressure drop is a well known problem with the Simplified Bernoulli equation. Both numerical (Casas et al., 2015; Donati et al., 2017) and patient studies (Baumgartner et al., 1999) have demonstrated this

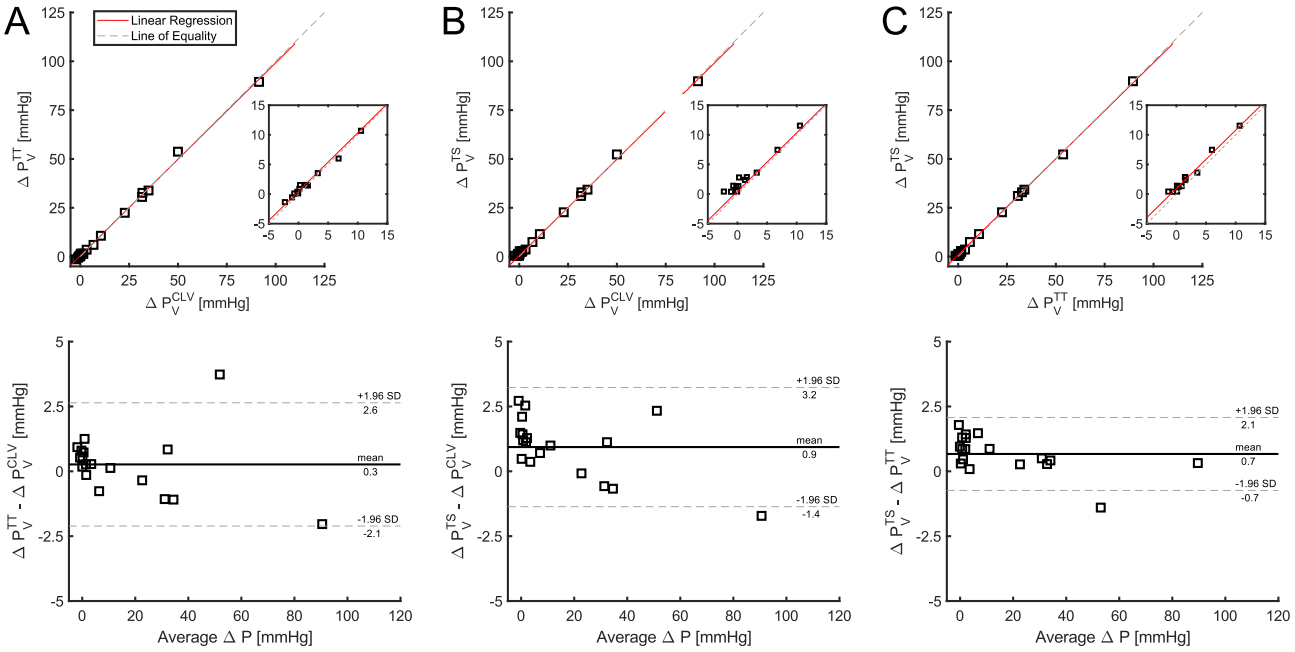

Fig. 8. Comparison between CFD models and their respective ΔP_V. Top row: scatter plot with linear regression results and line of equality. Bottom row: Bland-Altman of the difference. (A) Transient truncated model vs. full model ($R^2 = 0.998$); (B) truncated steady-state vs. full model ($R^2 = 0.998$); (C) truncated steady-state vs. truncated transient model ($R^2 = 0.999$).

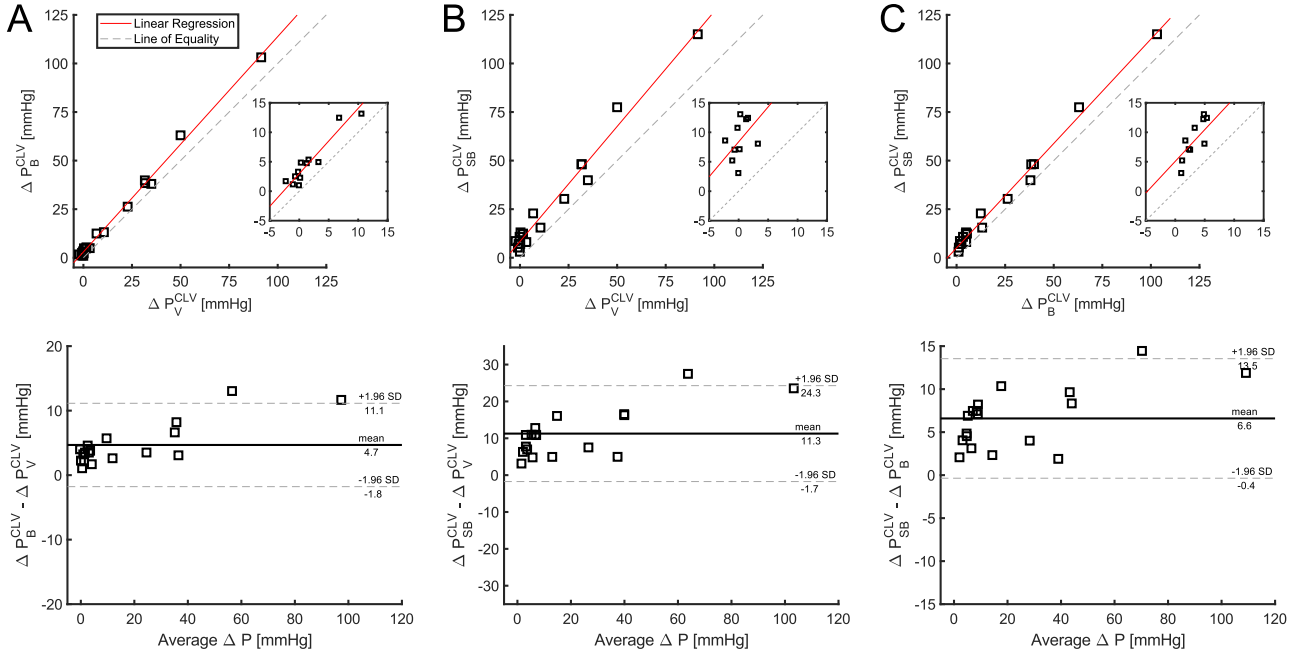

Fig. 9. Comparison between the Bernoulli estimates and pressure drops computed with the full CFD model. (A) Bernoulli estimate vs. full model ($R^2 = 0.995$); (B) simplifed Bernoulli ($4v^2$) estimate vs. full model ($R^2 = 0.973$); (C) simplified Bernoulli estimate vs. Bernoulli estimate ($R^2 = 0.991$).

overestimation. It should be noted that v_{max} is directly obtained from the simulated velocity field. Clinically, measurements are done with echocardiography, and additional sources of errors are likely, such as: poor spatial resolution, misalignment of the probe, or probe settings (Lui et al., 2005).

4.4. Limitations imaging and geometry

Segmentation with the SCDM is only possible for tri-cuspid AV's. Substantial segmentation errors are expected for bicuspid valves. Weese et al. showed that segmentation works in presence of calcifications (Weese et al., 2017). However, strong calcifications are likely to influence segmentation accuracy and blood flow. Hence, a thorough evaluation of segmentation accuracy is required. For example, it may be necessary to map patient-specific calcifications onto the SCDM.

Segmentation is performed on electrocardiography triggered CT images at 10% intervals of the R-R curve. It is assumed that the temporal resolution is sufficient to capture the (fully) open state of the AV. Poor temporal resolution may also cause over- or

underestimation of flow-rate. mitral regurgitation is not quantified, and patient flow-rates are likely overestimated. For example, patients with severe mitral valve regurgitation may see a regurgitant fraction of more than 50% (Zoghbi et al., 2017).

4.5. Limitations CFD

No valvular fluid-solid interaction is considered in this study due to the numerical challenges and lack of patient-specific material properties. It is expected that only local intraventricular and aortic flow fields are influenced. It is not expected that peak-systolic pressure drops and v_{max} are affected. Work by Astorino et al. supports this choice. Their work suggests that modeling the valve in the fixed open position yields an acceptable approximation for flow at peak systole, opposed to simulating the fully coupled fluid-solid interaction (Astorino et al., 2012).

The multi-cycle simulations that were performed on case 11 lacked the patient-specific mitral valve. As such, end-diastolic flow patterns may not be physiologically correct. For example, it has been shown that mitral valve opening dynamics and shape substantially influence end-diastolic vortex formation (Vasudevan et al., 2019). Whether the single-cycle approach is still acceptable in the presence of the segmented mitral valve has not been investigated.

5. Conclusion

An image-based CFD workflow of the AV and heart anatomy is presented. This workflow allows for the computation of a valve resistance index, that quantifies the contribution of the AV to the effective pressure drop from the LV to the AA. It is demonstrated that this index has the potential to complement existing measures, such as, v_{max} and the geometric AVA for patients that demonstrate discordant grading. Furthermore, it is shown that simplified CFD models provide a reasonable estimate of the aortic valve pressure drop at a given flow rate. However, at low-flow conditions simplifications to boundary conditions may not be justified, and more physiologically accurate inflow boundary conditions should be considered.

Declaration of Competing Interest

M.J.M.M. Hoeijmakers is an employee of ANSYS. J. Weese and I. Waechter-Stehle are employees of Philips.

Acknowledgements

This work was supported in part by the European Research Council Grant (Grant No.: 689617) and by the PLGrid Infrastructure. The authors would like to thank V. Morgenthaler for his valuable technical input.

References

Antiga, L., Piccinelli, M., Botti, L., Ene-Iordache, B., Remuzzi, A., Steinman, D.A., 2008. An image-based modeling framework for patient-specific computational hemodynamics. Med. Biol. Eng. Comput. 46, 1097–1112. https://doi.org/10.1007/s11517-008-0420-1.

Astorino, M., Hamers, J., Shadden, S.C., Gerbeau, J.-F., 2012. A robust and efficient valve model based on resistive immersed surfaces. Int. J. Numer. Meth. Biomed. Eng. 28, 937–959. https://doi.org/10.1002/cnm.2474.

Barber, D., Hose, D., 2005. Automatic segmentation of medical images using image registration: diagnostic and simulation applications. J. Med. Eng. Technol. 29, 53–63. https://doi.org/10.1080/03091900412331289889.

Baumgartner, H., Hung, J., Bermejo, J., Chambers, J.B., Edvardsen, T., Goldstein, S., Lancellotti, P., LeFevre, M., Miller, F., Otto, C.M., 2016. Recommendations on the echocardiographic assessment of aortic valve stenosis: a focused update from the european association of cardiovascular imaging and the american society of echocardiography. Euro. Heart J. – Cardiovasc. Imag. 18, 254–275. https://doi.org/10.1093/ehjci/jew335.

Baumgartner, H., Stefenelli, T., Niederberger, J., Schima, H., Maurer, G., 1999. overestimation of catheter gradients by doppler ultrasound in patients with aortic stenosis: a predictable manifestation of pressure recovery. J. Am. College Cardiol. 33, 1655–1661.

Bruening, J., Hellmeier, F., Yevtushenko, P., Kelm, M., Nordmeyer, S., Sündermann, S. H., Kuehne, T., Goubergrits, L., 2018. Impact of patient-specific LVOT inflow profiles on aortic valve prosthesis and ascending aorta hemodynamics. J. Comput. Sci. 24, 91–100. https://doi.org/10.1016/j.jocs.2017.11.005.

Casas, B., Lantz, J., Dyverfeldt, P., Ebbers, T., 2015. 4d flow MRI-based pressure loss estimation in stenotic flows: evaluation using numerical simulations. Magn. Reson. Med. 75, 1808–1821. https://doi.org/10.1002/mrm.25772.

Chambers, J.B., 2016. The assessment of aortic stenosis: echocardiography and beyond. Brit. J. Hospital Med. 77, 141–146. https://doi.org/10.12968/hmed.2016.77.3.141.

Chun, E.J., Choi, S.I., Lim, C., Park, K.-H., Chang, H.-J., Choi, D.-J., Kim, D.H., Lee, W., Park, J.H., 2008. Aortic stenosis: evaluation with multidetector CT angiography and MR imaging. Korean J. Radiol. 9, 439. https://doi.org/10.3348/kjr.2008.9.5.439.

Donati, F., Myerson, S., Bissell, M.M., Smith, N.P., Neubauer, S., Monaghan, M.J., Nordsletten, D.A., Lamata, P., 2017. Beyond bernoulli: Improving the accuracy and precision of noninvasive estimation of peak pressure drops. Circulation. Cardiovasc. Imag. 10. https://doi.org/10.1161/circimaging.116.005207.

Ecabert, O., Peters, J., Schramm, H., Lorenz, C., von Berg, J., Walker, M., Vembar, M., Olszewski, M., Subramanyan, K., Lavi, G., Weese, J., 2008. Automatic model-based segmentation of the heart in CT images. IEEE Trans. Med. Imag. 27, 1189–1201. https://doi.org/10.1109/tmi.2008.918330.

Ecabert, O., Peters, J., Walker, M.J., Ivanc, T., Lorenz, C., von Berg, J., Lessick, J., Vembar, M., Weese, J., 2011. Segmentation of the heart and great vessels in CT images using a model-based adaptation framework. Med. Image Anal. 15, 863–876. https://doi.org/10.1016/j.media.2011.06.004.

Eleid, M.F., Sorajja, P., Michelena, H.I., Malouf, J.F., Scott, C.G., Pellikka, P.A., 2013. Flow-gradient patterns in severe aortic stenosis with preserved ejection fraction. Circulation 128, 1781–1789. https://doi.org/10.1161/circulationaha.113.003695.

Eveborn, G.W., Schirmer, H., Heggelund, G., Lunde, P., Rasmussen, K., 2012. The evolving epidemiology of valvular aortic stenosis. the tromsøstudy. Heart 99, 396–400. https://doi.org/10.1136/heartjnl-2012-302265.

Garcia, J., Kadem, L., Larose, E., Clavel, M.-A., Pibarot, P., 2011. Comparison between cardiovascular magnetic resonance and transthoracic doppler echocardiography for the estimation of effective orifice area in aortic stenosis. J. Cardiovasc. Magn. Reson. 13, 25. https://doi.org/10.1186/1532-429x-13-25.

Grbic, S., Ionasec, R., Vitanovski, D., Voigt, I., Wang, Y., Georgescu, B., Navab, N., Comaniciu, D., 2012. Complete valvular heart apparatus model from 4d cardiac CT. Med. Image Anal. 16, 1003–1014. https://doi.org/10.1016/j.media.2012.02.003.

Hughes, S.W., D'Arcy, T.J., Maxwell, D.J., Saunders, J.E., Ruff, C.F., Chiu, W.S., Sheppard, R.J., 1996. Application of a new discreet form of gauss' theorem for measuring volume. Phys. Med. Biol. 41, 1809–1821.

Ionasec, R.I., Voigt, I., Georgescu, B., Wang, Y., Houle, H., Vega-Higuera, F., Navab, N., Comaniciu, D., 2010. Patient-specific modeling and quantification of the aortic and mitral valves from 4-d cardiac CT and TEE. IEEE Trans. Med. Imag. 29, 1636–1651. https://doi.org/10.1109/tmi.2010.2048756.

Lui, E.Y., Steinman, A.H., Cobbold, R.S., Johnston, K.W., 2005. Human factors as a source of error in peak doppler velocity measurement. J. Vasc. Surg. 42, 972.e1–972.e10. https://doi.org/10.1016/j.jvs.2005.07.014.

Menter, F.R., 1994. Two-equation eddy-viscosity turbulence models for engineering applications. AIAA J. 32, 1598–1605. https://doi.org/10.2514/3.12149.

Nicoud, F., Ducros, F., 1999. Subgrid-scale stress modelling based on the square of the velocity gradient tensor. Flow Turbul. Combust. 62, 183–200. https://doi.org/10.1023/a:1009995426001.

Nishimura, R.A., Otto, C.M., Bonow, R.O., Carabello, B.A., Erwin, J.P., Guyton, R.A., O'Gara, P.T., Ruiz, C.E., Skubas, N.J., Sorajja, P., Sundt, T.M., Thomas, J.D., 2014. 2014 AHA/ACC guideline for the management of patients with valvular heart disease. J. Am. College Cardiol. 63, e57–e185. https://doi.org/10.1016/j.jacc.2014.02.536.

Nkomo, V.T., Gardin, J.M., Skelton, T.N., Gottdiener, J.S., Scott, C.G., Enriquez-Sarano, M., 2006. Burden of valvular heart diseases: a population-based study. Lancet 368, 1005–1011. https://doi.org/10.1016/S0140-6736(06)69208-8.

Traeger, B., Srivatsa, S.S., Beussman, K.M., Wang, Y., Suzen, Y.B., Rybicki, F.J., Mazur, W., Miszalski-Jamka, T., 2015. Methodological inaccuracies in clinical aortic valve severity assessment: insights from computational fluid dynamic modeling of CT-derived aortic valve anatomy. Theor. Comput. Fluid Dyn. 30, 107–128. https://doi.org/10.1007/s00162-015-0370-9.

Vasudevan, V., Low, A.J.J., Annamalai, S.P., Sampath, S., Chin, C.-L., Ali, A.A.B., Yap, C.H., 2019. Role of diastolic vortices in flow and energy dynamics during systolic ejection. J. Biomech. 90, 50–57. https://doi.org/10.1016/j.jbiomech.2019.04.026.

Vogelgesang, A., Hasenfuss, G., Jacobshagen, C., 2017. Low-flow/low-gradient aortic stenosis-still a diagnostic and therapeutic challenge. Clin. Cardiol. 40, 654–659. https://doi.org/10.1002/clc.22728.

Weese, J., Lungu, A., Peters, J., Weber, F.M., Waechter-Stehle, I., Hose, D.R., 2017. CFD- and bernoulli-based pressure drop estimates: a comparison using patient anatomies from heart and aortic valve segmentation of CT images. Med. Phys. 44, 2281–2292. https://doi.org/10.1002/mp.12203.

Yang, C.-S., Marshall, E.S., Fanari, Z., Kostal, M.J., West, J.T., Kolm, P., Weintraub, W.S., Doorey, A.J., 2015. Discrepancies between direct catheter and echocardiography-based values in aortic stenosis. Catheter. Cardiovasc. Intervent. 87, 488–497. https://doi.org/10.1002/ccd.26033.

Zoghbi, W.A., Adams, D., Bonow, R.O., Enriquez-Sarano, M., Foster, E., Grayburn, P.A., Hahn, R.T., Han, Y., Hung, J., Lang, R.M., Little, S.H., Shah, D.J., Shernan, S., Thavendiranathan, P., Thomas, J.D., Weissman, N.J., 2017. Recommendations for noninvasive evaluation of native valvular regurgitation. J. Am. Soc. Echocardiogr. 30, 303–371. https://doi.org/10.1016/j.echo.2017.01.007.